NeuroImage 63 (2012) 936–946

Contents lists available at SciVerse ScienceDirect

NeuroImage

journal homepage: www.elsevier.com/locate/ynimg

Resting state FDG-PET functional connectivity as an early biomarker of Alzheimer's disease using conjoint univariate and independent component analyses

Paule-Joanne Toussaint [a,b,*], Vincent Perlbarg [a,b], Pierre Bellec [b,e], Serge Desarnaud [d], Lucette Lacomblez [a,c], Julien Doyon [b,e], Marie-Odile Habert [a,b,d], Habib Benali [a,b]
Benali, for the Alzheimer's Disease Neuroimaging Initiative. [1]

[a] Laboratoire d'Imagerie Fonctionnelle, UMR-S 678, INSERM-UPMC, Paris, France
[b] Laboratoire International de Neuroimagerie et Modélisation, Montréal, Qué., Canada
[c] Groupe Hospitalier Pitié-Salpêtrière, Service de Neurologie, Paris, France
[d] Groupe Hospitalier Pitié-Salpêtrière, Service de Médecine Nucléaire, Paris, France
[e] Centre de Recherche de l'Institut de Gériatrie de l'Université de Montréal, Montréal, Qué., Canada

ARTICLE INFO

Article history:
Accepted 30 March 2012
Available online 10 April 2012

Keywords:
Alzheimer's disease
Amnestic mild cognitive impairment
FDG-PET
Voxel-based group analysis
Independent component analysis
Support vector machine
Exploratory data-driven analysis

ABSTRACT

Imaging cerebral glucose metabolism with positron emission tomography (PET) in Alzheimer's disease (AD) has allowed for improved characterisation of this pathology. Such patterns are typically analysed using either univariate or multivariate statistical techniques. In this work we combined voxel-based group analysis and independent component analysis to extract differential characteristic patterns from PET data of glucose metabolism in a large cohort of normal elderly controls and patients with AD. The patterns were used in conjunction with a support vector machine to discriminate between subjects with mild cognitive impairment (MCI) at risk or not of converting to AD. The method was applied to baseline fluoro-deoxyglucose (FDG)-PET images of subjects from the ADNI database. Our approach achieved improved early detection and differentiation of typical versus pathological metabolic patterns in the MCI population, reaching 80% accuracy (85% sensitivity and 75% specificity) when using selected regions. The method has the potential to assist in the advance diagnosis of Alzheimer's disease, and to identify early in the development of the disease those individuals at high risk of rapid cognitive decline who could be candidates for new therapeutic approaches.

Introduction

Alzheimer's disease (AD) is classically diagnosed with clinical and cognitive assessments (McKhann et al., 1984). This diagnosis occurs late in the disease process (at the dementia stage), and it can only be confirmed post-mortem (Knopman et al., 2001). Patients suffering from AD at a prodromal stage are known to present a mild cognitive impairment (MCI; Dubois et al., 2007; Petersen et al., 1999, 2009). However, not all patients with amnestic MCI will develop AD, as MCI is a common syndrome that could be related to many causes other than AD (Petersen et al., 2009). Amnestic deficit in subjects with MCI is associated with the highest conversion rate to AD (Anchisi et al., 2005; Ganguli et al., 2004), but they constitute a heterogeneous population in which memory impairment may have causes other than AD. Identification of the AD process at earlier stages is critical for the development of disease modifying treatments, which would offer greater protection against further neuronal damage (Dubois and Albert, 2004; Petersen et al., 1999). Hypothetical models of AD progression assume a succession of underlying physiopathological events that lend themselves to (more of less early) intervention (Jack et al., 2010; Petersen et al., 2010). New diagnostic tools using imaging and other biomarkers aimed at identifying the disease at the pre-dementia (and ultimately asymptomatic) stage are being developed to complement and enhance the specificity of the clinical diagnosis. Imaging biomarkers can target disease identification (static) or disease evolution (dynamic) through structural, metabolic, or functional measurements (Aisen et al., 2010; Jack et al., 2010). Among these, positron emission tomography (PET) plays a major role in the characterisation and diagnosis of AD through its capacity to detect both the presence of early events and the progression of the disease. Molecular imaging with PET using amyloid-specific ligands can provide insight into the underlying pathophysiology by detecting the accumulation of Aβ42 and early neurodegeneration in AD and MCI (Jagust, 2004; Raji et al., 2008). Neuronal injury and

* Corresponding author at: Laboratoire d'Imagerie Fonctionnelle, UMR-S 678, INSERM-UPMC, LINeM, CHU Pitié-Salpêtrière, 91 boul. de l'Hôpital, 75634 Paris Cedex 13, France. Fax: +33 1 53 82 84 48.
E-mail address: PauleJoanne.Toussaint@imed.jussieu.fr (P.-J. Toussaint).

[1] Data used in preparation of this article were obtained from the Alzheimer's Disease Neuroimaging Initiative (ADNI) database (adni.loni.ucla.edu). As such, the investigators within the ADNI contributed to the design and implementation of ADNI and/or provided data but did not participate in analysis or writing of this report. A complete listing of ADNI investigators can be found at: http://adni.loni.ucla.edu/wp-content/uploads/how_to_apply/ADNI_Acknowledgement_List.pdf.

1053-8119/$ – see front matter © 2012 Elsevier Inc. All rights reserved.
doi:10.1016/j.neuroimage.2012.03.091

dysfunction can be captured by ^{18}F-labelled fluoro-deoxyglucose (FDG) PET imaging of changes in regional synaptic activity. These studies have revealed reduced glucose metabolism in the parieto-temporal and posterior cingulate cortices in AD (Eidelberg, 2009; Jagust et al., 2007; Minoshima et al., 1994, 1997; Mosconi, 2005; Pietrini et al., 1993; Rapoport et al., 1991). These regions are involved in memory processing and are structurally and functionally related to the default mode network, a set of brain regions that are activated during resting condition and tasks with low cognitive demand, and deactivated otherwise (Andrews-Hanna et al., 2007; Greicius et al., 2004). Such data contain a large amount of unique information that can be used for disease characterisation and classification. Both region-of-interest (ROI) and voxel-based approaches have been used in order to extract differential patterns from tracer metabolic data in healthy and diseased populations. Though ROI methods remain the most popular, the use of a limited number of pre-defined regions may not entirely reflect the spatial distribution patterns of physiological abnormalities (Fan et al., 2008). Univariate techniques (e.g. one-way ANOVA or *t*-test) have classically been used to analyse such data on a voxel-by-voxel basis (Friston et al., 1990). Recently, multivariate techniques (such as discriminant analysis or logistic regression) applied to metabolic data have received increasing attention (Habeck and Stern, 2010; Habeck et al., 2008; Kerrouche et al., 2006; Markiewicz et al., 2009, 2011a, 2011b; Scarmeas et al., 2004). This growing interest followed the observation that some relevant diagnostic patterns were better captured using multivariate approaches than univariate methods for the analysis (Scarmeas et al., 2004). Yet, association of these methods has not been tried in the extraction of differential patterns from imaging data for classification purposes.

In this work, we combined both techniques and performed a voxel-based analysis using two-sample *t*-test and independent component analysis (ICA), in conjunction with support vector machine (SVM), in order to explore the spatial properties of resting state glucose metabolism and evaluate the diagnostic value of FDG-PET data in prodromal AD pathology. The aim of the study was to test the hypothesis that glucose metabolic patterns observed in late stages of AD are already present at the prodromal stage, and to develop a multimodality classification tool for early diagnosis of AD based on imaging biomarkers derived from FDG-PET data spatial patterns (using *t*-test and ICA) combined with biological measurements (Apolipoprotein E) as well as scores from neuropsychological tests (MMSE, Adas, and Adas-cog).

The analysis was carried out in two steps. First, we performed voxel-based group comparisons as well as spatial ICA, and identified the most discriminating regions of metabolic deficits between healthy control and Alzheimer's disease populations. We then verified that these disease-specific patterns contain information that could be sufficient to characterise the pathology at its prodromal stage. For this, the resulting metabolic patterns from the previous step were applied to the MCI population (stable and converting to AD), combined with clinical and neuropsychological information, and used in a scheme for early diagnosis of AD involving classification with support vector machines.

Materials and methods

Data used in this work are taken from the Alzheimer's Disease Neuroimaging Initiative (ADNI) database (adni.loni.ucla.edu). The ADNI was launched in 2003 by the National Institute on Aging (NIA), the National Institute of Biomedical Imaging and Bioengineering (NIBIB), the Food and Drug Administration (FDA), private pharmaceutical companies and non-profit organisations. ADNI is a multicentre longitudinal cohort study of older adults, including cognitively normal elderly controls, amnestic MCI (including stable MCI and those converting to AD), and mildly affected AD patients at inclusion (Mueller et al., 2005) (for up-to-date information, see www.adni-info.org). The primary intent of ADNI has been to investigate whether serial MRI, PET, other biological markers, and clinical and neuropsychological assessment can be combined to evaluate the progression of MCI and early AD (Langbaum et al., 2009). Full details of subject recruitment, PET scanning protocols, and data preprocessing were published elsewhere (http://www.loni.ucla.edu/ADNI/; Jagust et al., 2010; Langbaum et al., 2009; Mueller et al., 2005) and only a brief account is given here.

Population description (demographics)

Subjects between the ages of 55 and 90 were enrolled in the ADNI study. Eligibility criteria were as follows (see Petersen et al., 2010, for a thorough description of participant recruitment and classification protocol). Normal elderly controls had a MMSE score of 24 or higher (Mini Mental State examination; Folstein et al., 1975), a clinical dementia rating (CDR) of 0 (Morris, 1993), and no diagnosis of neurological disease or psychiatric disorder. Amnestic MCI patients had a MMSE score of 24 or higher, a subjective memory complaint, objective memory loss measured by education adjusted scores on the Wechsler Memory Scale Logical Memory II, a CDR score of 0.5, absence of significant levels of impairment in other cognitive domains, preserved activities of daily living (ADLs), and an absence of dementia (Petersen et al., 2001). Participants with mild AD were enrolled if they had a MMSE score between 20 and 26 (inclusive), a CDR score of 0.5 or 1.0, and met NINCDS-ADRDA criteria for probable AD (McKhann et al., 1984).

A subset of the subjects having baseline FDG-PET scans (totalling 399) was used for our analysis. Based on their diagnosis at 18 months post-inclusion, groups of normal elderly controls (NEC; n = 80),

Table 1
Group distribution for voxel-based analysis. Fourty subjects were selected from the database for each group. Parameters were recorded at screening. Values are mean ± SD. Diagnosis at inclusion: NEC: cognitively normal elderly controls; MCIs: stable mild cognitive impairment; MCIc: converting mild cognitive impairment; pAD: probable Alzheimer's disease.

Diagnosis at inclusion	NEC	MCIs	MCIc	pAD
Number of subjects	80	40	40	80
Age (years)	76.4 ± 4.6 (65.6–86.6)	76.4 ± 4.2 (70.2–86.5)	76.4 ± 4.1 (70.3–86.0)	76.0 ± 6.3 (65.0–86.8)
Gender (male/female)	51/29	31/9	25/15	45/35
MMSE	29.0 ± 1.1	27.5 ± 1.8	26.8 ± 1.7	23.7 ± 2.1
Education (years)	16.0 ± 3.1	14.9 ± 3.2	16.4 ± 2.5	14.7 ± 3.2
Used for classification				
Number of subjects	40	40	40	40
Age (years)	75.5 ± 4.8 (65.6–86.0)	76.4 ± 4.2 (70.2–86.5)	76.4 ± 4.1 (70.3–86.0)	75.1 ± 5.6 (65.7–84.5)
Gender (male/female)	25/15	31/9	25/15	26/14
MMSE	29.1 ± 1.1	27.5 ± 1.8	26.8 ± 1.7	23.7 ± 2.0
Education (years)	16.3 ± 2.9	14.9 ± 3.2	16.4 ± 2.5	14.8 ± 3.5

patients with mild cognitive impairment that had remained stable (MCIs; n = 40) or had converted to AD (MCIc; n = 40) during the two-year follow-up, as well as patients diagnosed with probable AD (pAD; n = 80) were matched for age, sex, and MMSE score distributions (Table 1). The matched subsets were mainly used to avoid the confounding factors of age, sex and MMSE distribution on the extraction of discriminating patterns, such that these patterns would not be obtained because of the inherent differences of these variables, but only because of the difference between controls and Alzheimer patients. Our methodology should therefore ensure that the extracted regions (and thus ultimately prediction using these regions) would not be founded on – and potentially be biased by – the means of these variables.

FDG-PET data acquisition and processing

Baseline resting state positron emission tomographic scans of glucose metabolism (FDG-PET) from the ADNI database were used for this study. All baseline PET scans were acquired according to one of three different standardised protocols: 1) dynamic 30-min, six frame (5 min each) acquisitions starting 30 min post ^{18}F-labelled fluoro-deoxyglucose (^{18}F-FDG) injection, 2) quantitative 60-min dynamic protocol with continuous scanning from injection time to calculate absolute glucose metabolic rate using an arterial input function measured in the carotid, and 3) a single-frame 30-min acquisition starting 30 min post-injection for scanners without dynamic capability. Subjects were asked to remain still and keep awake with eyes open looking straight ahead for the entire acquisition.

The co-registered, averaged, normalised (standardised image and voxel size) and smoothed to a uniform resolution (8 mm full-width at half-maximum) PET images (also known as “post-processed #4” data) were downloaded from the LONI repository (Joshi et al., 2009; http://www.loni.ucla.edu/ADNI). Images were then spatially normalised to a study specific template based on 80 FDG-PET scans of elderly controls, which were transformed to the MNI PET and MRI templates space, scaled, and averaged using SPM5 (method adapted from Gispert et al., 2003). Spatial normalisation of all images involved a 12-parameter affine transformation, followed by nonlinear iterative spatial transformation as provided in SPM5 software package (http://www.fil.ion.ucl.ac.uk/spm/). Data were then scaled in intensity using the global mean value of the average value of the pons, a region known to be preserved in AD and shown to adequately reflect inter-individual variability (Buchert et al., 2005). The pontine area was approximated to a spherical region with 10 mm radius centered at [0 -26 -33] mm by region growing (using MarsBAR). In each subject, the average PET count value in the pons was determined in the spatially normalised PET image. This value was used to divide each voxel intensity of the PET image of that subject, following what voxel-wise *t* statistics for between group comparisons were computed using procedures in SPM5.

Analysis

Characteristic patterns of interest were obtained from 80 cognitively normal elderly controls and 80 patients with probable AD using the methods described below. Masks were created using SPM MarsBAR tool (http://marsbar.sourceforge.net/) on a subset of 40 controls and 40 AD patients (see Table 1) and applied to FDG-PET images of the remaining subjects from the database not included in this part of the analysis to extract individual voxel intensities within the selected regions of interest, thus avoiding circularity in the prediction analysis.

Cluster-based analysis

Whole brain analyses were performed by computing voxel-based statistics using SPM5, implemented in Matlab 7 (MathWorks Inc., Sherborn, MA). Two-sample *t*-tests controlling for age, sex, education, scanner type, and scanning centre were used to identify significant regional cerebral glucose metabolism in each patient group relative to elderly controls. An absence of gender differences in metabolic activity of AD patients was reported previously (Minoshima et al., 1997). While groups were matched for their mean age, sex, and education, we included these as covariates in the analysis to remove the residual variance that could still be explained by these variables at the individual level. Intensity scaling was performed as described above (see Section 2), and grey matter probability threshold was set to 0.8 (SPM default). Only voxels surviving false discovery rate (FDR) correction for the entire volume at a p value below 0.001 (minimum extent 30 voxels) were accepted in the statistical analysis between AD patients and healthy controls, in order to avoid false positive results. The resulting *t*-maps were examined for determining individual areas of significant metabolic changes as well as for defining disease-specific patterns. The regional patterns were assessed via a correlation analysis, where partial correlation coefficients (Pearson) between regions were calculated.

Component-based analysis

Voxel-based methods such as the one described above are massively univariate: each voxel is tested in isolation of the rest of the brain. By contrast, multivariate methods such as spatial independent analysis (sICA) have the ability to capture the spatially distributed covariation of FDG PET measurements across subjects. In addition, ICA does not rely on a specific shape for the haemodynamic response. In functional MRI, this technique has been found to identify patterns that match well with the maps of brain regions involved in distinct families of cognitive processes (Smith et al., 2009). The differences found in a specific ICA network are thus easier to interpret in terms of associated cognitive functions (and potential deficits) than the results of voxel-based statistics. Also, ICA may be more sensitive than voxel-based statistics in some situations because they capture spatially distributed patterns (Rombouts et al., 2009). We therefore used spatial independent component analysis (ICA) in order to extract additional regions of interest that may have been missed by the two-sample *t*-test. Resting state FDG-PET data from elderly controls and AD patients were included simultaneously in the spatial ICA (see Appendix A for a short review) for the purpose of obtaining regions of greatest coherent activation that would be common to both groups. To do so, the FDG-PET volumes from all subjects were concatenated. We performed spatial ICA using sICA, an algorithm from a locally developed toolbox for analysing brain networks (NetBrainWork, Perlbarg et al., 2007). This program uses an InfoMax algorithm, following dimension reduction by principal component analysis (PCA). The method for estimating the number of components uses a Bayesian model selection (Minka, 2000). In brief, ICA was first performed to identify signal- from noise-related components using a priori masks of vessels and cerebrospinal fluid. Redundant components were then eliminated by PCA. We chose to extract 40 components so as not to miss out on any network of regions of interest, and to avoid the increase in noise-related components observed with increasing number of extracted components. The components of interest were selected by comparing the extracted components to 18 spatial templates of functional networks identified from resting-state fMRI group analysis on healthy controls, and thresholding high correlation coefficients (for uncorrected $p<0.001$ and voxel extent ≥ 30; Perlbarg et al., 2007).

The analysis produced a series of independent components (ICs) with associated curve plots. The curve represents the average metabolic changes across subjects within the combined spatial map, and each point corresponds to the PET scan of a different subject. Thus, for a given component, each point on the associated curve describes how strongly the spatial map for that component is related to a particular individual FDG-PET image.

As this analysis does not differentiate between groups, we looked for correlations between a template of the default mode network

(DMN), and the spatial patterns obtained previously. Since the DMN was shown to have diagnostic power in AD (Greicius et al., 2004; Koch et al., 2010; Sorg et al., 2007; Zhou et al., 2010), this added a priori spatial information and allowed to better identify potentially discriminant regions. This should help in the selection of discriminant components. For this, we computed the correlation coefficients between regions, while controlling for the DMN. Regions with correlation above 0.50 were selected for the analysis of the PET data from the NEC and pAD subjects not included in the discriminant pattern selection process, as well as data from the MCI population (MCIs and MCIc). The latter were not used for the original derivation of the *t*-maps and ICA patterns. Voxel values were averaged over each selected region of interest, and these numbers were entered into the SVM.

Support vector machine

Average ROI values calculated with the above masks were used as features for classification using support vector machines. Support vector machines (SVM) are a class of discriminant function originally developed in statistical machine learning theory as a linear binary classifier (Vapnik, 1995). Given a set of training data, SVMs try to maximise the separation margin defined by the distance between a hyperplane and the closest data samples.

Detailed description of SVMs can be found elsewhere (Boser et al., 1992; Cortes and Vapnik, 1995). In the present work we have used a non-linear binary classifier SVM (C-SVM) with a Gaussian kernel (using libSVM Matlab toolbox, http://www.csie.ntu.edu.tw/~cjlin/libsvm; Chang and Lin, 2011). Two-sample *t*-test and spatial ICA served as feature reduction steps. A grid search was performed for model parameter optimisation. Ten-fold cross-validation was used to evaluate the performance of each parameter combination in the classifier training scheme. Added feature selection was based on the average weight of support vectors, keeping all those vectors having more than 50% of the maximum weight attributed during training of the classifier. Performance of the classification was tested using a leave-one-out approach, where the classifier is trained with all but one instance (subject) of the database. The process was repeated such that each subject was used as validation data once, and the success rate (accuracy) was computed from the number of correctly classified subjects. In addition to determining accuracy, the classifier performance was evaluated by calculating specificity (reflecting true negative rate) and sensitivity (reflecting true positive rate).

Results

Identification of discriminant FDG patterns

The two-sample *t*-test maps from the analysis of NEC compared to diseased groups are shown in Fig. 1. Though differences between AD patients and normal elderly controls were significant up to a stringent threshold $p<0.001$ corrected for family-wise error (FWE), results are presented at a less conservative FDR-corrected p-value<0.001 to include more areas. The uncorrected p-value<0.001 (cluster extent 30 voxels) in Fig. 1 is used for consistency with comparisons of NEC versus stable and converting MCI subjects. For the comparison of NEC with stable MCI subjects at baseline, regions of observed hypometabolism in MCIs were medial frontal (MF), anterior cingulate (AC), right superior temporal (STR), and bilateral superior parietal areas. In addition to the above cited areas (AC excepted), MCI converters also showed hypometabolism in left ST, bilateral inferior temporal and inferior parietal, right middle frontal (MFR), precuneus–posterior cingulate area (PPC), and left parahippocampal (pHL) areas. Hypometabolic patterns for patients with probable AD involved more frontal areas (medial and bilateral middle frontal). The patterns also included bilateral middle parietal and middle temporal areas, bilateral fusiform, left and right thalamic areas, PPC, and bilateral parahippocampal areas. Significant hypometabolism was found in bilateral inferior temporal, bilateral superior parietal and posterior cingulate areas when MCI

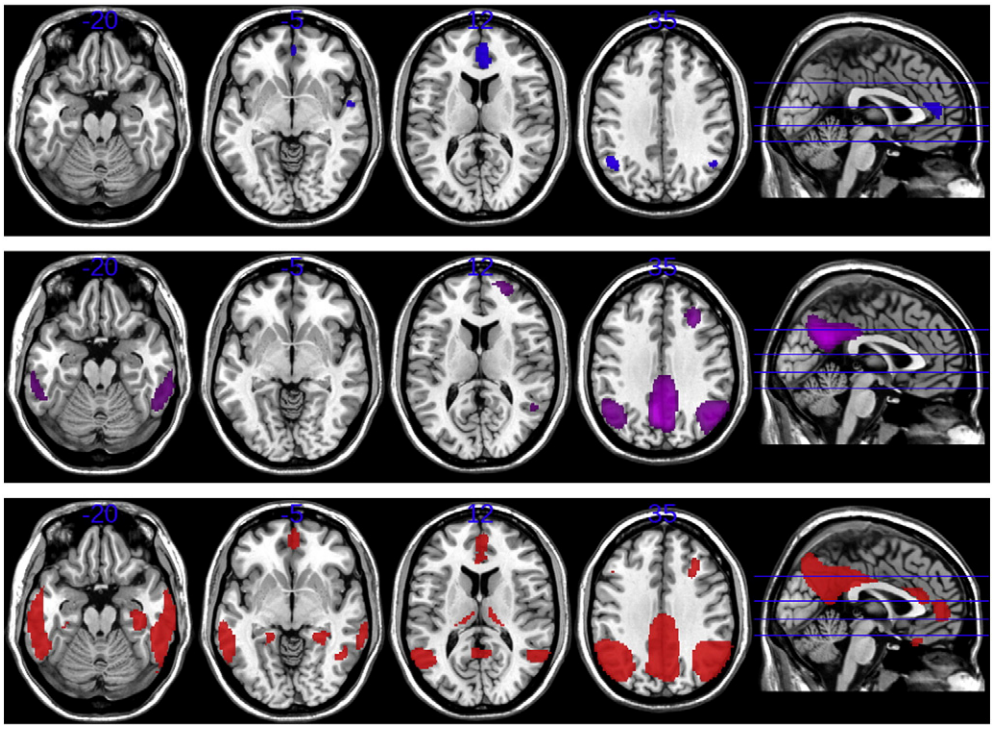

Fig. 1. *t*-statistic maps for the comparison of cognitively normal elderly controls with subjects presenting with stable MCI (top), MCI converters (middle), and patients with AD (bottom). Results are presented at a cluster significance level of $p<0.001$ (uncorrected) with minimum extent of 30 voxels. Regions of hypometabolism in non-converting MCI subjects are more frontal, with inferior parietal involvement. As the MCI convert to AD, hypometabolic regions become more posterior, involving inferior temporal areas and the PCC. For established AD patients compared to controls, hypometabolic patterns are more scattered. NEC: cognitively normal elderly controls; MCIs: stable mild cognitive impairment; MCIc: converting mild cognitive impairment; pAD: probable Alzheimer's disease.

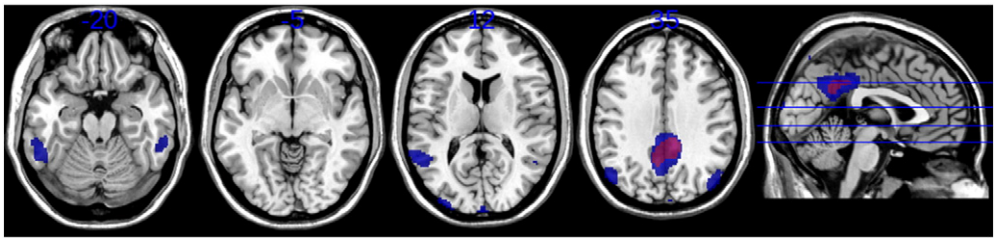

Fig. 2. *t*-statistic maps for the comparison of subjects presenting with stable MCI, and MCI converters showing hypometabolism mainly in posterior areas. Results are presented for uncorrected $p<0.001$ (red areas) and $p<0.01$ (blue areas).

converters were compared to stable subjects (Fig. 2). Peak characteristics for areas showing significant hypometabolism in pAD compared to NEC that were used for creating a mask of discriminating regions of interest are listed in Table 2.

Extraction of coherent metabolic patterns

Of the 40 components calculated from the spatial ICA on NEC and pAD data combined, eight were selected as having patterns that were significantly altered in the AD patients compared to normal elderly controls when these were contrasted with a set of 18 templates derived from resting-state functional MRI studies on healthy controls. Components extracted by spatial ICA are superposed and presented in Fig. 3. Areas with increased intensity represent regions of co-occurring changes in FDG patterns between the groups included in the analysis. The regions showing most coherent metabolic activity included the frontal, temporal and posterior areas (parietal and PPC) cited above for the two-sample *t*-test in addition to more posterior cortical areas, including visual association areas. Frontal areas had highly concomittant metabolic activity with each other (executive control), and with temporal (ventral attentional) or posterior (PPC, medial visual component) regions. Highly coherent metabolism was observed between the more posterior regions (including medial visual), parahippocampal areas and basal ganglia. Parietal areas were concomittantly correlated with temporal and parahippocampal areas (salient component), or with lateral visual area. Metabolic activity in the PPC was most coherent with that in the superior temporal, parietal and left basal ganglia areas (default mode, limbic component). There were also coherent metabolic changes between the temporal regions, right medial frontal, and right parahippocampal areas (dorsal attentional, basal ganglia components). To assess the regional similarity within spatial patterns of each independent component, selected ICs were regressed on a standardised template of the default mode network obtained from resting state fMRI studies. Component outliers were excluded at this stage, and the component spatially closest to the DMN served for the analysis. The *t* statistic map from the comparison of NEC with pAD was also found to be close to the DMN when compared to the template for verification.

Exploratory correlation analysis of hypometabolic regions

We further explored the spatial properties of the FDG PET data by performing a correlation analysis on the mean values of the discriminating ROIs. For each group, correlations between regions constituting each pattern (extracted from two-sample *t*-test and ICA) were calculated while controlling for areas of the DMN. These correlations are therefore partial correlations with respect to the areas of the DMN. Controls were compared to AD patients and MCI subjects, and regions with correlations above $+/-0.5$ were considered to bring additional information and were included into the SVM. Results of this analysis are shown in Figs. 4 and 5.

All groups showed highly correlated changes within frontal areas (medial frontal, superior and middle frontal areas) with highest correlated metabolic changes observed for the MCI converter group ($p<0.05$). Changes were more correlated between all frontal regions and temporal areas in MCI converters. On average, with respect to the control group, parietal and temporal areas were more highly correlated for converters than for stable MCI (Figs. 4 and 5, top right). Parietal and frontal areas were more highly correlated ($p<0.05$) for AD patients compared to subjects with MCI (Fig. 4). However, strongest correlation was observed in subjects with MCI between metabolic changes in left lateral parietal and left inferior temporal areas, though the correlation in these areas was highly significant in all groups ($p<0.05$). Subjects with stable MCI had significant strongly correlated changes of metabolic activity between left and right superior temporal areas, and left parahippocampal area. AD patients alone showed highly significant correlated metabolic changes between superior temporal and parahippocampal areas bilaterally.

There was progressive involvement of PPC with other areas, from posterior to anterior regions, with evolving stages of the disease. Comparing stable MCI to NEC, significant metabolic change in the PPC was associated with hypometabolism in left and right lateral parietal areas, and with changes in parahippocampal as well as inferior and medial temporal areas ($p<0.05$; Figs. 4 and 5, top and middle left). When comparing stable and converting MCI (Fig. 4, top right), PPC showed very significant correlated metabolic changes with bilateral superior temporal areas ($p<0.05$). Correlation between the PPC

Table 2
Between group analysis: Comparison of hypometabolism between AD patients (n = 40) and normal elderly controls (n = 40) at p(FDR)<0.001, for minimum cluster extent of 50 voxels.

Local maximum (mm)			*t*-value	Label	Cluster volume
x	y	z	Voxel-level	(Most probable from AAL toolbox)	(# voxels)
−4	−54	26	6.84	Precuneus–posterior cingulate	1511
−40	−66	42	6.60	Left parietal	2170
42	−54	42	6.68	Right parietal	1397
−62	−32	−18	5.40	Left inferior/middle temporal	976
64	−40	−16	4.52	Right inferior/middle temporal	112
24	−2	−32	4.78	Right superior temporal	55
30	−40	−6	4.76	Right para-hippocampal area	51

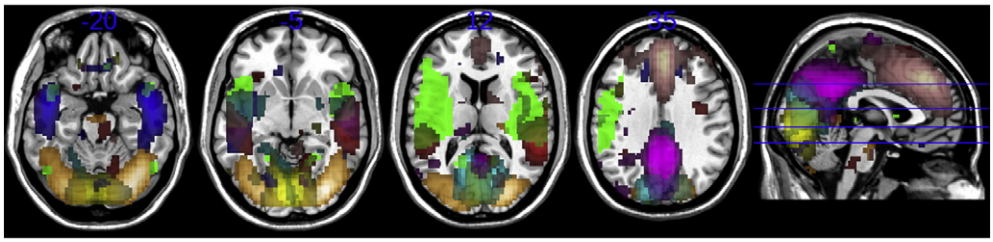

Fig. 3. Resulting eight component maps determined from combined groups of controls and AD patients. Spatial ICA was performed using NetBrainWork with 40 classes (p(unc)<0.001). The extracted components are in concordance with those found in resting state fMRI studies. Red: dorsal attentional, basal ganglia; Blue: ventral attentional; Green: salient; Violet: limbic, DM; Yellow: medial visual; Cyan: posterior cingulate; Pink: executive control; Gold: lateral visual.

and bilateral temporal and parahippocampal areas slightly increased (ns), but there was decreased correlation between hypometabolism in the PPC and right lateral parietal area ($p<0.05$). For subjects with converting MCI and AD patients (Figs. 4 and 5, bottom right), metabolic changes in the parietal were more highly correlated with changes in prefrontal areas in AD (mainly middle and superior frontal, $p<0.05$). Correlated changes between the lateral and superior temporal areas slightly increased, while they continued to decrease with parahippocampal areas (mainly left), and no differences were observed with inferior and middle temporal areas bilaterally.

Pattern discrimination using SVM

Classification results for different combinations of FDG-PET imaging and clinical features are shown in Table 3. Only the best performing set for selected feature combinations are presented for each group. Discrimination of controls and AD patients was achieved with more than 97% accuracy in most combinations of clinical features only (MMSE, ADAS, and ADAS-cog). Using the same combinations of clinical features, the best accuracy achieved for discriminating between MCIs and MCIc was 62% (using MMSE and ADAS). By comparison, regions selected from the FDG-PET maps based on the correlation analysis (left lateral parietal, bilateral inferior temporal, and right parahippocampal areas) yielded 80% accuracy for classification within the MCI population. Using the same regions for discrimination of NEC from pAD subjects resulted in 75% accuracy (with 65% sensitivity and 85% specificity). However, when medial and superior frontal (left and right) were used with bilateral inferior and superior temporal areas, classification was achieved with 92.5% accuracy for NEC and pAD, whereas the same areas yielded 55% accuracy (60% sensitivity, 50% specificity) when distinguishing MCIs vs MCIc. Combining clinical scores and imaging features from the FDG-PET improved the classification for NEC versus pAD. Discrimination for the MCI population became more specific with the combination of clinical and imaging features, albeit with a small loss in sensitivity, but this was corrected with the addition of more regions (parietal and temporal).

Discussion

Our study explored voxel-based group comparison and independent component analyses of baseline FDG-PET data for the extraction of imaging features to be used in conjunction with a classification scheme in order to evaluate the potential of connectivity within regional patterns of FDG-PET as an early biomarker of AD. Results showed that FDG hypometabolic patterns from two-sample *t*-test evolve in a predetermined fashion with disease progression, and that these patterns strongly influence the specificity of the discrimination between different stages of AD. These hypometabolic patterns were shown to include areas constituting the default mode network (DMN), a resting network that has been consistently found to be impaired during resting state in MCI and AD (Bai et al., 2008; Greicius et al., 2004; Rombouts et al., 2005; Sorg et al., 2007) beyond the more general age-related disruption of large-scale networks (Andrews-Hanna et al., 2007). Evidence suggests that the default mode network is important to memory function as it is functionally disrupted in MCI and AD (Miller et al., 2008).

The areas identified with the two-sample *t*-test and spatial ICA are in concordance with the literature describing the clinical presentation of the disease, and include regions involved in memory processing that are known to be affected early in AD. The selected components are thought to be associated with the clinical presentation of the disease because they are composed of regions that present greatest network changes (defined by ICA) between the two populations. The prefrontal cortex has been shown to be involved in working memory and is also thought to play a key role by contributing with attentional input and information integration (Dudkin et al., 2006; Müller and Knight, 2006). Medial temporal cortices contain fundamental circuits for declarative memory (Ranganath, 2006; Squire, 1999), and occipital and inferior temporal areas are related to object recognition (Müller and Knight, 2006). Patterns also included areas implicated in language and visual processing. Regional metabolic deficits in the left posterior cingulate cortex and the left hippocampal/parahippocampal area were specifically related to impairments in verbal episodic memory in a resting FDG-PET study in AD (Desgranges et al., 1998). Lesions to the left inferior frontal and insular areas are known to produce apraxia of speech, and damage to anterior temporal regions leads to semantic memory deficits (Gorno-Tempini et al., 2004). Medial and lateral visual areas and fusiform gyrus are involved in face recognition and spatial navigation, and impaired visuo-spatial information processing is thought to develop early in AD (Duffy, 2009; Rizzo and Nawrot, 1998; Silverman et al., 1994; Tetewsky and Duffy, 1999).

Patterns from spatial ICA agreed with known networks that have been observed in resting state functional MRI studies of control subjects and AD patients (Damoiseaux et al., 2006). Of the 18 networks compared with the extracted components, all were matched (by multi-dimensional scaling), though they appeared to be broken down in two or more components in some cases. In addition, these coherent patterns were very similar to those typically observed in dementia of the Alzheimer type, with highly coherent hypometabolism in the temporal, parietal, and frontal areas, indicating a higher contribution from these regions to discrimination between AD patients and controls (Rombouts et al., 2009).

Both two-sample *t*-test and spatial ICA patterns closely resembled the default mode network, with the known distribution of memory-related areas. The pattern of reduced activity in AD has been described in posterior associative cortices, extending to different frontal areas, with a relative preservation of metabolism in the primary cortices and subcortical structures using PET or fMRI (Herholz et al., 2002; Rombouts et al., 2009).

Hypometabolic patterns of Fig. 1 show that medial pre-frontal areas are affected early in individuals with MCI, followed by progressive involvement of more posterior regions (left and right lateral parietal, parahippocampal, PPC, temporal) in subjects with MCI at risk of converting to AD. As the disease progresses, temporal areas become

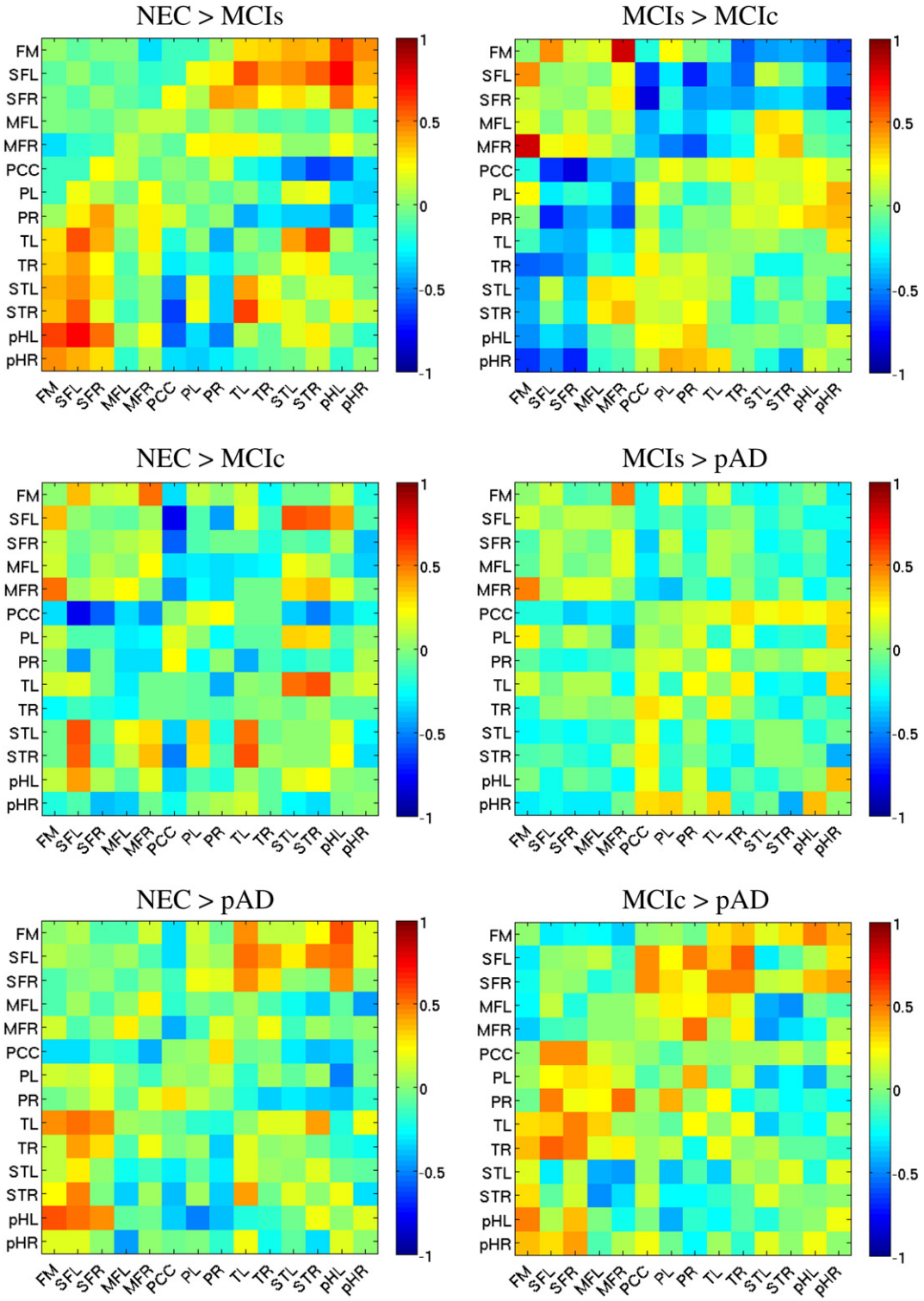

Fig. 4. Comparison of correlation coefficients between groups for the *t*-map clusters. The mask created from the contrast map was applied to each subject and the average ROI values between groups were compared. MF: medial frontal; SFL/SFR: superior frontal left/right; MFL/MFR: middle frontal left/right; PCC: precuneus-posterior cingulate; PL/PR: parietal left/right; TL/TR: temporal (inferior and middle) left/right; STL/STR: superior temporal left/right; pHL/pHR: para-hippocampal left/right.

more involved. Thus from a state of mild cognitive impairment at risk (or not) of conversion to AD, the glucose hypometabolic pattern begins as medial pre-frontal, then appears to follow a posterior parieto-occipito-temporal circuit (including the PCC) to finally become predominantly temporo-parietal, with participation of frontal areas, in long-established AD (Fig. 5). Whether or not hippocampi would be more involved at an earlier (stable to converting MCI) or later stage (MCI converter to AD) of the disease remains to be verified, although from this study the former seems more plausible as there was highly correlated co-activation of parahippocampal with parietal and temporal areas when subjects with stable MCI were compared to the converters (Figs. 1 and 4).

When the masks derived from comparison of these patterns were applied to the different populations included in the study, increased correlated metabolic activity within frontal and temporal areas was observed for stable MCI (Fig. 4). In MCI converters, correlation

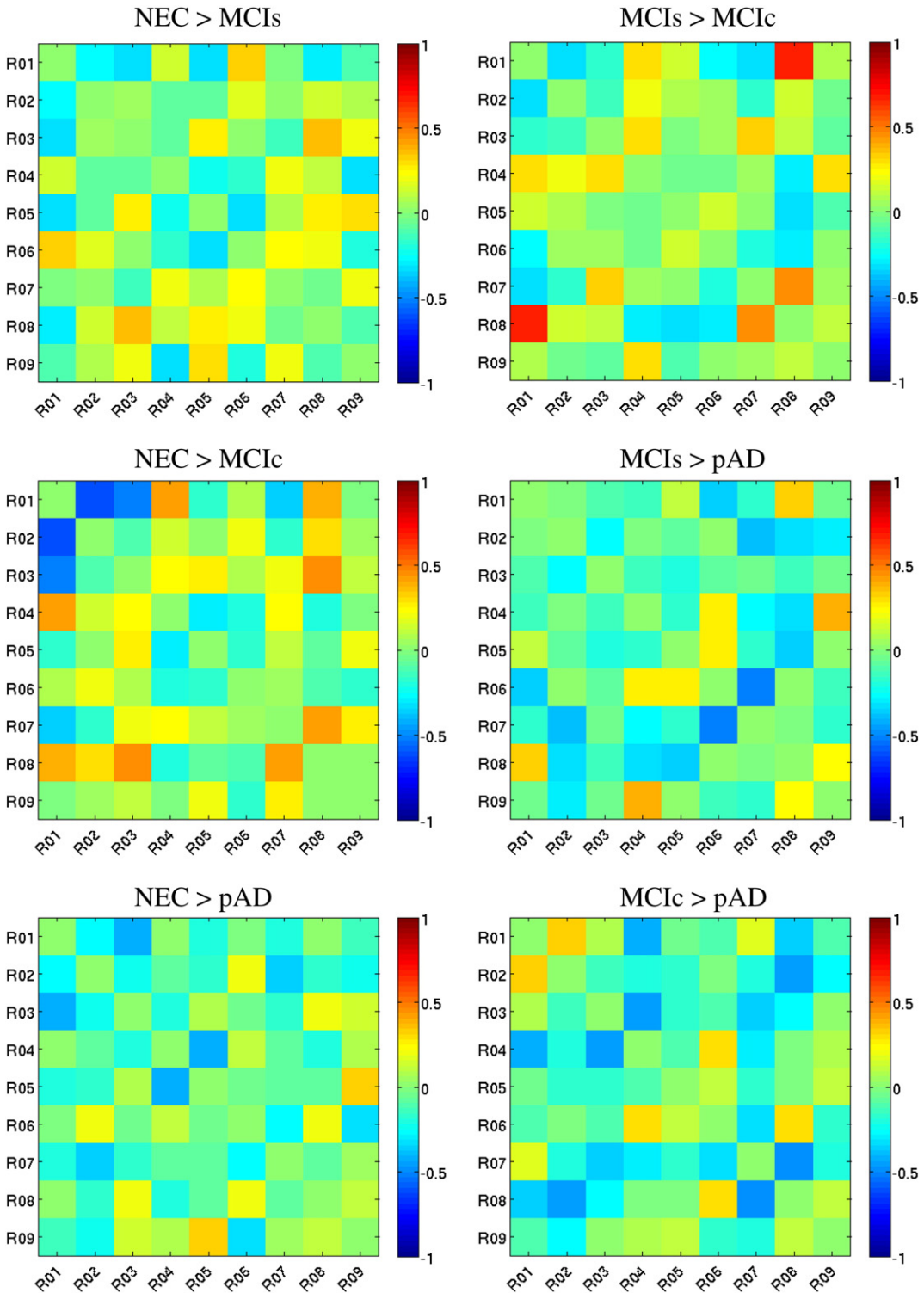

Fig. 5. Comparison of correlation coefficients between groups for a selected component of interest. SFo (R01): superior frontal orbital gyrus; Prc (R02, R05, R08): precuneus; MC (R03): middle cingulum; Ang (R04): angular gyrus; MT (R06): middle temporal gyrus; Ins (R07): insula; PcL (R09): paracentral lobule.

between frontal and temporal areas increased, while there was decreased correlation within the temporal areas. This was reversed in the AD population as fronto-temporal correlations decreased, and correlations within the temporal area increased, which could signal the breakdown of cognitive compensation mechanisms. Increased correlations between temporal and hippocampal areas were also observed in these subjects. There were previous reports of strong interconnection of the posterior cingulate with hippocampal formation in individuals at risk for developing AD, probably as a compensatory response for memory encoding mechanisms (Andrews-Hanna et al., 2007; Greicius et al., 2004; Sperling et al., 2009; Vincent et al., 2006). It is also known that the posterior cingulate has reciprocal anatomical connections with the prefrontal (superior and middle frontal) and orbitofrontal cortices, the inferior parietal lobule, the superior temporal sulcus, and the parahippocampal gyrus (Pandya et al., 1981). In the present work, such interconnections are portrayed by the increased correlation between PPC and parahippocampal areas in the stable MCI population compared to NEC (Fig. 4, top left). This

Table 3
Classification with SVM using a RBF kernel with leave-one-out cross-validation. Listed are results for combinations of imaging (resting FDG-PET) and clinical (MMSE, ADAS, ADAS-cog, Apoε) features for differentiating MCIs and MCIc. Regions were selected based on correlations and co-activation (ICA) patterns, and support vectors with weight above 50% were included in the model. COI: component of interest; MF: medial frontal; SFL/SFR: superior frontal left/right; MFL/MFR: middle frontal left/right; PCC: precuneus-posterior cingulate; PL/PR: parietal left/right; TL/TR: temporal (inferior and middle) left/right; STL/STR: superior temporal left/right; pHL/pHR: para-hippocampal left/right. MMSE: Mini Mental State Examination; ADAS: Alzheimer's Disease Assessment Scale; ADAS-cog: cognitive sub-scale; Apoε: apolipoprotein E.

	Accuracy	Sensitivity	Specificity	Features
NEC vs pAD				
t-map	0.92	0.90	0.95	MF,SFL/R,TL/R,STL/R
Cognitive scores	1.00	1.00	1.00	MMSE, ADAS; ≥0.97 other
Cognitive, Apoε	1.00	1.00	1.00	MMSE, Apoε; ≥0.92 other
t-map, clinical	1.00	1.00	1.00	With MMSE, ADAS, or Apoε
t-map, COIs	0.91	0.84	1.00	44 clusters
MCIs vs MCIc				
t-map	0.80	0.85	0.75	PL, TL/R, pHL
Cognitive scores	0.62	0.55	0.70	MMSE, ADAS
Cognitive, Apoε	0.68	0.65	0.70	MMSE, ADAS, ADAS-cog, Apoε
t-map, clinical	0.80	0.75	0.85	PL, TL/R, pHL, MMSE, ADAS, Apoε
t-map, cognitive	0.82	0.85	0.80	(P,T,ST)L/R, pHL, MMSE, ADAS
t-map, COIs	0.60	0.38	0.73	47 clusters

co-activation decreases in MCI converters, and disappears altogether in AD patients compared to NEC as the compensation mechanism presumably collapses. On the other hand, correlations of PPC with prefrontal areas appear only when MCI converters are compared to AD patients, associated with a decreased correlation with parahippocampal area, indicating that information from the frontal and parietal association cortices may no longer be relayed to the hippocampus.

Based on these observations, the areas with most discriminative potential would be: 1. frontal (medial and superior) and temporal regions for distinguishing AD from healthy controls (fronto-temporal connections), and 2. lateral parietal, temporal, and parahippocampal areas for discriminating between stable and converting MCI subjects (temporo-parietal connections).

These interpretations should be regarded with caution. The accuracy of multicentric (heterogeneous) data samples, such as are used in the present work, can be affected by the type of PET scanner and the image reconstruction method. These have been shown to impact on multivariate analyses such as PCA, which is used as a dimension reduction step in our ICA approach (Markiewicz et al., 2011b). Both *t*-test and ICA methods perform equally well for identification of discriminating voxel patterns, but when there are differences in connectivity between brain regions ICA detects more active voxels at rest than *t*-test (Sato et al., 2008). Though they are classically used to analyse FDG-PET data, univariate techniques such as *t*-test analysis may not be using all the information available in the datasets. These techniques tend to ignore functional correlations among brain structures and they may be lacking in both sensitivity and specificity (Kerrouche et al., 2006). On the other hand, multivariate techniques may bring some improvement in sensitivity, but they still lack in specificity. ICA searches the regions of greatest coherent changes in activity in the data, which might as well stand for anatomical variability within the studied population rather than changes that could be attributed to AD. Thus, the power of ICA is not necessarily superior to *t*-tests, but is a function of the relationship between changes in mean activation and the nature of the underlying connectivity structure(s).

Classification of imaging data in AD, including FDG-PET, has been achieved using SVMs in conjunction with either univariate or multivariate techniques for feature selection (Salas-Gonzalez et al., 2010; Zhang et al., 2011). In the present work, we combined the use of both approaches to take advantage of their respective sensitivity and specificity in order to increase the differentiating capabilities of the classification (Table 3). The obtained results for differentiating AD patients from cognitively normal control subjects are in line with classifier performances reported in the literature (Table 4). It is interesting to note that cognitive testing alone might as well be used for classification of a population of cognitively normal controls against well-established AD. The interest of our method is in its application to earlier stages of AD, and the resulting improved differentiation of cognitively stable MCI subjects from those at risk of converting to AD using the FDG-PET biomarkers in combination with cognitive scores, with good sensitivity and specificity. We have concentrated on the regions

Table 4
Classification with SVM using a RBF kernel with leave-one-out cross-validation (unmatched subjects). Listed are results for combinations of imaging (resting FDG-PET) and clinical (MMSE, ADAS, ADAS-cog, Apoε) features. Regions were selected based on correlations and co-activation (ICA) patterns, and support vectors with weight above 50% were included in the model. MF: medial frontal; SFL/SFR: superior frontal left/right; MFL/MFR: middle frontal left/right; PCC: precuneus-posterior cingulate; PL/PR: parietal left/right; TL/TR: temporal (inferior and middle) left/right; STL/STR: superior temporal left/right; pHL/pHR: para-hippocampal left/right. MMSE: Mini Mental State Examination; ADAS: Alzheimer's Disease Assessment Scale; ADAS-cog: cognitive sub-scale; Apoε: apolipoprotein E.

	Accuracy	Sensitivity	Specificity	Features
NEC vs pAD				
t-map	0.87	0.88	0.86	14 clusters
COIs	0.89	0.84	0.95	33 clusters
Cognitive, Apoε	0.99	0.98	1.00	MMSE, Apoε; ≥0.89 other
t-map, COIs	0.91	0.84	1.00	44 clusters
t-map, COIs, clinical	0.98	0.96	1.00	13 clusters
MCIs vs MCIc				
t-map	0.53	0.31	0.65	13 clusters
COIs	0.56	0.25	0.75	36 clusters
Cognitive, Apoε	0.67	0.12	0.98	MMSE, ADAS, ADAS-cog, Apoε
t-map, COIs	0.60	0.38	0.73	47 clusters
t-map, COIs, clinical	0.60	0.25	0.80	19 clusters

constituting the DMN because they are involved in memory processing and are known to be affected early in AD. Other components extracted with spatial ICA, such as visual or attentional components, could also be included in the classification scheme as a means to improve discrimination.

Our results are encouraging, and argue for the need of a multimodality assessment of subjects with cognitive complaints.

Acknowledgments

Financial support was partially provided by grants from the IFR-49. Data collection and sharing for this project was funded by the Alzheimer's Disease Neuroimaging Initiative (ADNI) (National Institutes of Health Grant U01 AG024904). ADNI is funded by the National Institute on Aging, the National Institute of Biomedical Imaging and Bioengineering, and through generous contributions from the following: Abbott; Alzheimer's Association; Alzheimer's Drug Discovery Foundation; Amorfix Life Sciences Ltd.; AstraZeneca; Bayer HealthCare; BioClinica, Inc.; Biogen Idec Inc.; Bristol-Myers Squibb Company; Eisai Inc.; Elan Pharmaceuticals Inc.; Eli Lilly and Company; F. Hoffmann-La Roche Ltd and its affiliated company Genentech, Inc.; GE Healthcare; Innogenetics, N.V.; Janssen Alzheimer Immunotherapy Research & Development, LLC.; Johnson & Johnson Pharmaceutical Research & Development LLC.; Medpace, Inc.; Merck & Co., Inc.; Meso Scale Diagnostics, LLC.; Novartis Pharmaceuticals Corporation; Pfizer Inc.; Servier; Synarc Inc.; and Takeda Pharmaceutical Company. The Canadian Institutes of Health Research is providing funds to support ADNI clinical sites in Canada. Private sector contributions are facilitated by the Foundation for the National Institutes of Health (www.fnih.org). The grantee organisation is the Northern California Institute for Research and Education, and the study is coordinated by the Alzheimer's Disease Cooperative Study at the University of California, San Diego. ADNI data are disseminated by the Laboratory for Neuro Imaging at the University of California, Los Angeles. This research was also supported by NIH grants P30 AG010129 and K01 AG030514, and the Dana Foundation.

Appendix A. Independent component analysis

The main assumption behind ICA is that each data sample is a linear mixture of a set of statistically independent signal sources (glucose hypometabolism in the present case) and is then unmixed by means of a linear mixing model according to their statistical independence measured by mutual information (Hyvärinen et al., 2001). Assuming that $\mathbf{x}$ is a pixel vector in an image (here FDG-PET) which is linearly mixed by a set of p statistically independent signal sources $s_1, \ldots, s_p$ by means of a mixing matrix $\mathbf{A}$ as: $\mathbf{x}=\mathbf{As}$, where $\mathbf{A}$ is an $L\times p$ mixing matrix and $\mathbf{s}=(s_1, \ldots, s_p)^{\mathrm{T}}$ is a p-dimensional signal source vector of brain glucose metabolism that must be separated. The aim of ICA is to unmix the observed mixed signal source $\mathbf{x}$ using the above equation to find an unmixing matrix $\mathbf{W}$ such that the p unknown signal sources representing brain tissue clusters in the signal source vector $\mathbf{s}$ can be separated by the following unmixing equation: $\mathbf{s}=\mathbf{Wx}$. Analysis by independent components has shown great promise in fMRI, a method that provides task-related information in time series of MR brain images. Since the image data for fMRI are collected along a temporal sequence where the number of data samples, denoted by L, is generally greater than p, the number of signal sources of the task-related information to be separated, the ICA aims at solving an overdetermined system with $L<p$. In this case, there are more data samples to be used for data analysis than signal sources to be separated. A general approach uses dimensionality reduction to bring the value of L down to p in order to obtain a square unmixing matrix $\mathbf{W}$.

On the other hand, in PET image classification, one scan corresponds to a single data sample. As a result, the number $L=1$ used for PET image analysis in our experiment is smaller than the signal sources representing the different brain tissue clusters (such as grey matter, white matter, cerebrospinal fluid, abnormal tissue, etc.). In this case, we have to solve an over-determined problem, as opposed to the under-determined problem that must be solved with fMRI data, where there is at least one IC which must accommodate multiple tissue clusters due to the lack of data dimensionality. To resolve this dilemma where there are insufficient ICs to deal with the large number of brain tissue (signal sources) while preserving the ability of ICA to enhance contrast brain images, the support vector machine has been proposed for incorporation in conjunction with the ICA to improve its separation abilities (Chai et al., 2010).

References

Aisen, P.S., Petersen, R.C., Donohue, M.C., Gamst, A., Raman, R., Thomas, R.G., Walter, S., Trojanowski, J.Q., Shaw, L.M., Beckett, L.A., Jack Jr., C.R., Jagust, W., Toga, A.W., Saykin, A.J., Morris, J.C., Green, R.C., Weiner, M.W., the ADNI, 2010. Clinical core of the Alzheimer's Disease Neuroimaging Initiative: Progress and plans. Alzheimers Dement. 6, 239–246.

Anchisi, D., Borroni, B., Franceschi, M., Kerrouche, N., Kalbe, E., Beuthien-Beumann, B., Kappa, S., Lenz, O., Ludecke, S., Marcone, A., Mielke, R., Ortelli, P., Padovani, A., Pelati, O., Pupi, A., Scarpini, E., Weisenbach, S., Herholz, K., Salmon, E., Holthoff, V., Sorbi, S., Fazio, F., Perani, D., 2005. Heterogeneity of brain glucose metabolism in mild cognitive impairment and clinical progression to Alzheimer disease. Arch. Neurol. 62, 1728–1733.

Andrews-Hanna, J.R., Snyder, A.Z., Vincent, J.L., Lustig, C., Head, D., Raichle, M.E., Buckner, R.L., 2007. Disruption of large-scale brain systems in advanced aging. Neuron. 56, 924–937.

Bai, F., Zhang, Z., Yu, H., Shi, Y., Yuan, Y., Zhu, W., Zhang, X., Qian, Y., 2008. Default-mode network activity distinguishes amnestic type mild cognitive impairment from healthy aging: a combined structural and resting-state functional MRI study. Neurosci. Lett. 438, 111–115.

Boser, B.E., Guyon, I.M., Vapnik, V.N., 1992. A training algorithm for optimal margin classifiers. In: Proceedings of the Fifth Annual Workshop on Computational Learning Theory. COLT '92. ACM, New York, pp. 144–152.

Buchert, R., Wilke, F., Chakrabarti, B., Martin, B., Brenner, W., Mester, J., Clausen, M., 2005. Adjusted scaling of FDG positron emission tomography images for statistical evaluation in patients with suspected Alzheimer's disease. J. Neuroimaging 15, 348–355.

Chai, J.W., Chi-Chang Chen, C., Chiang, C.M., Ho, Y.J., Chen, H.M., Ouyang, Y.C., Yang, C.W., Lee, S.K., Chang, C.I., 2010. Quantitative analysis in clinical applications of brain MRI using independent component analysis coupled with support vector machine. J. Magn. Reson. Imaging 32, 24–34.

Chang, C.C., Lin, C.J., 2011. LIBSVM: A library for support vector machines. ACM Trans. Intell. Syst. Technol. 2, 1–27.

Cortes, C., Vapnik, V., 1995. Support vector network. Mach. Learn. 20, 273–297.

Damoiseaux, J.S., Rombouts, S.A., Barkhof, F., Scheltens, P., Stam, C.J., Smith, S.M., Beckmann, C.F., 2006. Consistent resting-state networks across healthy subjects. Proc. Natl. Acad. Sci. U. S. A. 103, 13848–13853.

Desgranges, B., Baron, J.C., de la Sayette, V., Petit-Taboué, M.C., Benali, K., Landeau, B., Lechevalier, B., Eustache, F., 1998. The neural substrates of memory systems impairment in Alzheimer's disease: A PET study of resting brain glucose utilization. Brain 121, 611–631.

Dubois, B., Albert, M.L., 2004. Amnestic MCI or prodromal Alzheimer's disease? Lancet Neurol. 3, 246–248.

Dubois, B., Feldman, H.H., Jacova, C., Dekosky, S.T., Barberger-Gateau, P., Cummings, J., Delacourte, A., Galasko, D., Gauthier, S., Jicha, G., Meguro, K., O'brien, J., Pasquier, F., Robert, P., Rossor, M., Salloway, S., Stern, Y., Visser, P.J., Scheltens, P., 2007. Research criteria for the diagnosis of Alzheimer's disease: revising the NINCDS-ADRDA criteria. Lancet Neurol. 6, 734–746.

Dudkin, K.N., Chueva, I.V., Makarov, F.N., Bich, T.G., Roher, A.E., 2006. Disorders of learning and memory processes in a monkey model of Alzheimer's disease: The role of the associative area of the cerebral cortex. Neurosci. Behav. Physiol. 36, 789–799.

Duffy, C.J., 2009. Visual motion processing in aging and Alzheimer's disease: Neuronal mechanisms and behavior from monkeys to man. Ann. N. Y. Acad. Sci. 1170, 736–744.

Eidelberg, D., 2009. Metabolic brain networks in neurodegenerative disorders: a functional imaging approach. Trends Neurosci. 32, 548–557.

Fan, Y., Resnick, S.M., Wu, X., Davatzikos, C., 2008. Structural and functional biomarkers of prodromal Alzheimer's disease: a high-dimensional pattern classification study. NeuroImage 41, 277–285.

Folstein, M.F., Folstein, S.E., McHugh, P.R., 1975. Mini Mental State. J. Psychiatr. Res. 12, 189–198.

Friston, K.J., Frith, C.D., Liddle, P.F., Dolan, R.J., Lammertsma, A.A., Frackowiak, R.S.J., 1990. The relationship between global and local changes in PET scans. J. Cereb. Blood Flow Metab. 10, 458–466.

Ganguli, M., Dodge, H.H., DeKosky, S.T., 2004. Mild cognitive impairment, amnestic type: an epidemiologic study. Neurology 63, 115–121.

Gispert, J.D., Pascau, J., Reig, S., Martínez-Lázaro, R., Molina, V., García-Barreno, P., Desco, M., 2003. Influence of the normalization template on the outcome of statistical parametric mapping of PET scans. Neuroimage 19, 601–612.

Gorno-Tempini, M.L., Dronkers, N.F., Rankin, K.P., Ogar, J.M., Phengrasamy, L., Rosen, H.J., Johnson, J.K., Weiner, M.W., Miller, B.L., 2004. Cognition and anatomy in three variants of primary progressive aphasia. Ann. Neurol. 55, 335–346.
Greicius, M.D., Srivastava, G., Reiss, A.L., Menon, V., 2004. Default-mode network activity distinguishes Alzheimer's disease from healthy aging: Evidence from functional MRI. Proc. Natl. Acad. Sci. 13, 4637–4642.
Habeck, C., Foster, N.L., Perneczky, R., Kurz, A., Alexopoulos, P., Koeppe, R.A., Drzezga, A., Stern, Y., 2008. Multivariate and univariate neuroimaging biomarkers of Alzheimer's disease. Neuroimage 40, 1503–1515.
Habeck, C., Stern, Y., 2010. Multivariate data analysis for neuroimaging data: Overview and application to Alzheimer's disease. Cell Biochem. Biophys. 58, 53–67.
Herholz, K., Salmon, E., Perani, D., Baron, J.C., Holthoff, V., Frolich, L., Schonknecht, P., Ito, K., Mielke, R., Kalbe, E., Zundorf, G., Delbeuck, X., Pelati, O., Anchisi, D., Fazio, F., Kerrouche, N., Desgranges, B., Eustache, F., Beuthien-Baumann, B., Menzel, C., Schroder, J., Kato, T., Arahata, Y., Henze, M., Heiss, W.D., 2002. Discrimination between Alzheimer dementia and controls by automated analysis of multicenter FDG PET. Neuroimage 17, 302–326.
Hyvärinen, A., Karhunen, J., Oja, E., 2001. Independent component analysis. Wiley, New York.
Jack, C.R., Knopman, D., Jagust, W.J., Shaw, L.M., Aisen, P.S., Weiner, M.W., Petersen, R.C., Trojanowski, J.Q., 2010. Hypothetical model of dynamic biomarkers of the Alzheimer's pathological cascade. Lancet Neurol. 9, 119–128.
Jagust, W., 2004. Molecular imaging in Alzheimer's disease. NeuroRX 1, 206–212.
Jagust, W., Reed, B., Mungas, D., Ellis, W., DeCarli, C., 2007. What does fluorodeoxyglucose PET imaging add to a clinical diagnosis of dementia? Neurology 69, 871–877.
Jagust, W.J., Bandy, D., Chen, K., Foster, N.L., Landau, S.M., Mathis, C.A., Price, J.C., Reiman, E.M., Skovronsky, D., Koeppe, R.A., ADNI, 2010. The Alzheimer's Disease Neuroimaging Initiative positron emission tomography core. Alzheimers Dement. 6, 221–229.
Joshi, A., Koeppe, R.A., Fessler, J.A., 2009. Reducing between scanner differences in multi-center PET studies. Neuroimage 46, 154–159.
Kerrouche, N., Herholz, K., Mielke, R., Holthoff, V., Baron, J.C., 2006. ^{18}FDG PET in vascular dementia: differentiation from Alzheimer's disease using voxel-based multivariate analysis. J. Cereb. Blood Flow Metab. 26, 1213–1221.
Knopman, D.S., DeKosky, S.T., Cummings, J.L., Chui, H., Corey-Bloom, J., Relkin, N., Small, G.W., Miller, B., Stevens, J.C., 2001. Practice parameter: diagnosis of de- mentia (an evidence-based review) report of the Quality Standards Subcommittee of the American Academy of Neurology. Neurology 56, 1143–1153.
Koch, W., Teipel, S., Mueller, S., Buerger, K., Bokde, A.L., Hampel, H., Coates, U., Reiser, M., Meindl, T., 2010. Effects of aging on default mode network activity in resting state fMRI: does the method of analysis matter? Neuroimage 51, 280–287.
Langbaum, J.B.S., CHen, K., Lee, W., Reschke, C., Bandy, D., Fleisher, A.S., Alexander, G.E., Foster, N.L., Weiner, M.W., Koeppe, R.A., Jagust, W., Reiman, E.M., the ADNI, 2009. Categorical and correlational analyses of baseline fluorodeoxyglucose positron emission tomography images from the Alzheimer's Disease Neuroimaging Initiative (ADNI). Neuroimage 45, 1107–1116.
Markiewicz, P.J., Matthews, J.C., Declerck, J., Herholz, K., 2009. Robustness of multivariate image analysis assessed by resampling techniques and applied to FDG-PET scans of patients with Alzheimer's disease. Neuroimage 46, 472–485.
Markiewicz, P.J., Matthews, J.C., Declerck, J., Herholz, K., 2011a. Robustness of correlations between PCA of FDG-PET scans and biological variables in healthy and demented subjects. Neuroimage 56, 782–787.
Markiewicz, P.J., Matthews, J.C., Declerck, J., Herholz, K., Alzheimer's Disease Neuroimaging Initiative (ADNI), 2011b. Verification of predicted robustness and accuracy of multivariate analysis. Neuroimage 56, 1382–1385.
McKahnn, G., Drachman, D., Folstein, M., Katzman, R., Price, D., Stadlan, E.M., 1984. Clinical diagnosis of Alzheimer's disease: report of the NINCDS-ADRDA Work Group under the auspices of Department of Health and Human Services Task Force on Alzheimer's Disease. Neurology 34, 939–944.
Miller, S.L., Celone, K., DePeau, K., Diamond, E., Dickerson, B.C., Rentz, D., Pihlajamäki, M., Sperling, R.A., 2008. Age-related memory impairment associated with loss of parietal deactivation but preserved hippocampal activation. PNAS 105, 2181–2186.
Minka, T.P., 2000. Automatic choice of dimensionality for PCA. MLPCS 514, MIT Media Laboratory Perceptual Computing Section. December.
Minoshima, S., Koeppe, R.A., Frey, K.A., Kuhl, D.E., 1994. Anatomic standardization: Linear scaling and nonlinear warping of functional brain images. J. Nucl. Med. 35, 1528–1537.
Minoshima, S., Giordani, B., Berent, S., Frey, K.A., Foster, N.L., Kuhl, D.E., 1997. Metabolic reduction in the posterior cingulate cortex in very early Alzheimer's disease. Ann. Neurol. 42, 85–94.
Morris, J.C., 1993. The Clinical Dementia Rating (CDR): Current version and scoring rules. Neurology 43, 2412–2414.
Mosconi, L., 2005. Brain glucose metabolism in the early and specific diagnosis of Alzheimer's disease. Eur. J. Nucl. Med. Mol. Imaging 32, 486–510.
Mueller, S.G., Weiner, M.W., Thal, L.J., Petersen, R.C., Jack, C.R., Jagust, W.J., Trojanowski, J.Q., Toga, A.W., Beckett, L., 2005. Ways toward an early diagnosis in Alzheimer's disease: the Alzheimer's Disease Neuroimaging Initiative (ADNI). Alzheimers Dement. 1, 55–66.
Müller, N.G., Knight, R.T., 2006. The functional neuroanatomy of working memory: Contributions of human brain lesion studies. Neuroscience 139, 51–58.
Pandya, D.N., Hoesen, G.W.V., Mesulam, M.M., 1981. Efferent connections of the cingulate gyrus in the rhesus monkey. Exp. Brain Res. 42, 319–330.
Perlbarg, V., Bellec, P., Anton, J.L., Pelegrini-Issac, M., Doyon, J., Benali, H., 2007. CORSICA: correction of structured noise in fMRI by automatic identification of ICA components. Magn. Reson. Imaging 25, 35–46.
Petersen, R.C., Smith, G.E., Waring, S.C., Ivnik, R.J., Tangalos, E.G., Kokmen, E., 1999. Mild cognitive impairment: clinical characterization and outcome. Arch. Neurol. 56, 303–308.
Petersen, R.C., Stevens, J.C., Ganguli, M., Tangalos, E.G., Cummings, J.L., DeKosky, S.T., 2001. Practice parameter: early detection of dementia: mild cognitive impairment (an evidence-based review). Neurology 56, 1133–1142.
Petersen, R.C., Roberts, R.O., Knopman, D.S., Boeve, B.F., Geda, Y.E., Ivnik, R.J., Smith, G.E., Jack Jr., C.R., 2009. Mild cognitive impairment: ten years later. Arch. Neurol. 66, 1447–1455.
Petersen, R.C., Aisen, P.S., Beckett, L.A., Donohue, M.C., Gamst, A.C., Harvey, D.J., Jack Jr., C.R., Jagust, W.J., Shaw, L.M., Toga, A.W., Trojanowski, J.Q., Weiner, M.W., 2010. Alzheimer's Disease Neuroimaging Initiative (ADNI): Clinical characterization. Neurology 74, 201–209.
Pietrini, P., Azari, N.P., Grady, C.L., Salerno, J.A., Gonzales-Aviles, A., Heston, L.L., Pettigrew, K.D., Horwitz, B., Haxby, J.V., Schapiro, M.B., 1993. Pattern of cerebral metabolic interactions in a subject with isolated amnesia at risk for Alzheimer's disease: a longitudinal evaluation. Dementia 4, 94–101.
Raji, C.A., Becker, J.T., Tsopelas, N.D., Price, J.C., Mathis, C.A., Saxton, J.A., Lopresti, B.J., Hoge, J.A., Ziolko, S.K., DeKosky, S.T., Klunk, W.E., 2008. Characterizing regional correlation, laterality and symmetry of amyloid deposition in mild cognitive impairment and Alzheimer's disease with Pittsburgh Compound B. J Neurosc Methods 172, 277–282.
Ranganath, C., 2006. Working memory for visual objects: complementary roles of inferior temporal, medial temporal, and prefrontal cortex. Neuroscience 139, 277–289.
Rapoport, S.I., Horwitz, B., Grady, C.L., Haxby, J.V., DeCarli, C., Schapiro, M.B., 1991. Abnormal brain glucose metabolism in Alzheimer's disease, as measured by positron emission tomography. Adv. Exp. Med. Biol. 291, 231–248.
Rizzo, M., Nawrot, M., 1998. Perception of movement and shape in Alzheimer's disease. Brain 121, 2259–2270.
Rombouts, S.A., Barkhof, F., Goekoop, R., Stam, C.J., Scheltens, P., 2005. Altered resting state networks in mild cognitive impairment and mild Alzheimer's disease: An fMRI study. Hum. Brain Mapp. 26, 231–239.
Rombouts, S.A., Damoiseaux, J.S., Goekoop, R., Barkhof, F., Scheltens, P., Smith, S.M., Beckmann, C.F., 2009. Model-free group analysis shows altered BOLD fMRI networks in dementia. Hum. Brain Mapp. 30, 256–266.
Salas-Gonzalez, D., Goórriz, J.M., Ramírez, J., Illan, I.A., Lopez, M., Segovia, F., Chaves, R., Padilla, P., Puntonet, C.G., 2010. Feature selection using factor analysis for Alzheimer's diagnosis using 18F-FDG PET images. Med. Phys. 37, 6084–6095.
Sato, J.R., Mourão-Miranda, J., Martin, M.G.M., Amaro Jr., E., Morettin, P.A., Brammer, M.J., 2008. The impact of functional connectivity changes on support vector machines mapping of fMRI data. J. Neurosci. Methods 172, 94–104.
Scarmeas, N., Habeck, C.G., Zarahn, E., Anderson, K.E., Park, A., Hilton, J., Pelton, G.H., Tabert, M.H., Honig, L.S., Moeller, J.R., Devanand, D.P., Stern, Y., 2004. Covariance PET patterns in early Alzheimer's disease and subjects with cognitive impairment but no dementia: utility in group discrimination and correlations with functional performance. Neuroimage 23, 35–45.
Silverman, S.E., Tran, D.B., Zimmerman, K.M., Feldon, S.E., 1994. Dissociation between the detection and perception of motion in Alzheimer's disease. Neurology 44, 1814–1818.
Smith, S.M., Fox, P.T., Miller, K.L., Glahn, D.C., Fox, P.M., Mackay, C.E., Filippini, N., Watkins, K.E., Toro, R., Laird, A.R., Beckmann, C.F., 2009. Correspondence of the brain's functional architecture during activation and rest. Proc. Natl. Acad. Sci. 106, 13040–13045.
Sorg, C., Riedl, V., Mühlau, M., Calhoun, V.D., Eichele, T., Läer, L., Drzezga, A., Förstl, H., Kurz, A., Zimmer, C., Wohlschläger, A.M., 2007. Selective changes of resting-state networks in individuals at risk for Alzheimer's disease. Proc. Natl. Acad. Sci. U. S. A. 104, 18760–18765.
Sperling, R.A., Laviolette, P.S., O'Keefe, K., O'Brien, J., Rentz, D.M., Pihlajamaki, M., Marshall, G., Hyman, B.T., Selkoe, D.J., Hedden, T., Buckner, R.L., Becker, J.A., Johnson, K.A., 2009. Amyloid deposition is associated with impaired default network function in older persons without dementia. Neuron. 63, 178–188.
Squire, L.R., 1999. Memory and the hippocampus: a synthesis from findings with rats, monkeys, and humans. Psychol. Rev. 99, 195–231.
Tetewsky, S., Duffy, C.J., 1999. Visual loss and getting lost in Alzheimer's disease. Neurology 52, 958–965.
Vapnik, V., 1995. The nature of statistical learning theory. Springer-Verlag, New York.
Vincent, J.L., Snyder, A.Z., Fox, M.D., Shannon, B.J., Andrews, J.R., Raichle, M.E., Buckner, R.L., 2006. Coherent spontaneous activity identifies a hippocampal-parietal memory network. J. Neurophysiol. 96, 3517–3531.
Zhang, D., Wang, Y., Zhou, L., Yuan, H., Shen, D., Alzheimer's Disease Neuroimaging Initiative, 2011. Multimodal classification of Alzheimer's disease and mild cognitive impairment. Neuroimage 55, 856–867.
Zhou, J., Greicius, M.D., Gennatas, E.D., Growdon, M.E., Jang, J.Y., Rabinovici, G.D., Kramer, J.H., Weiner, M., Miller, B.L., Seeley, W.W., 2010. Divergent network connectivity changes in behavioral variant frontotemporal dementia and Alzheimer's disease. Brain 133, 1352–1367.